Supporting Information

Electrowetting-Assisted Printing of 3D-Architectured Microelectrodes inside Flexible Piezoelectric Films for Sensitive, Robust Responses to Bending Deformation

Chao Yan[1], *Xiangming Li*[1,2]*, *Zhengjie Yang*[1], *Xiaopei Wang*[1], *Hao Ran*[1], *Ruolin Zhang*[1], *Hongmiao Tian*[1], *Chunhui Wang*[1], *Xiaoliang Chen*[1,2], *Jinyou Shao*[1,2]*

1 Micro-/Nano-Technology Research Center, State Key Laboratory for Manufacturing Systems Engineering, Xi'an Jiaotong University, Xi'an, Shaanxi 710049, China

2 Xiangming Li, Xiaoliang Chen, Jinyou Shao, Frontier Institute of Science and Technology (FIST), Xi'an Jiaotong University, Xi'an, Shaanxi 710049, China

* Correspondence author: E-mail: (X.L.) xiangmingli@xjtu.edu.cn; (J.S.) jyshao@xjtu.edu.cn

This file includes:

Supplementary Table

Supplementary Figures

Captions for Supplementary Videos

Other Supplementary Material for this manuscript includes the following:

Supplementary Videos S1

Table S1. Comparison of performance of polymer-based piezoelectric devices

Piezoelectric materials	Electrode layout	Number of bending cycles	Output fluctuation	Enhancement strategy	Output enhancement (U/U_0)
PVDF @ BTO-Gr[1]	Parallel plate electrodes	1800	~ 40%	Composite	~ 4.4
P(VDF-TrFE)/BTO @ PMMA[2]	Parallel plate electrodes	6000	~ 21.5%	Interfacial modulation	~2.2
P(VDF-TrFE)/ BTO @ C[3]	Parallel plate electrodes	1000	N/A	Interfacial modulation	~ 3
PVDF@ ZnO[4]	Parallel plate electrodes	5000	~ 14.3%	Composite	~ 2.06
PZT network @ PDMS[5]	Parallel plate electrodes	20000	~ 15.2% (top sensor)	N/A	N/A
			~ 19.1% (bottom sensor)	N/A	N/A
P(VDF-TrFE)/ PCNPs @ TDPA[6]	Parallel plate electrodes	10000	~ 18.3%	Interfacial modulation	1.6
P(VDF-TrFE) [7]	Tilted electrode	N/A	N/A	Electrode design	~ 2.05
P(VDF-TrFE) [8]	3D interdigital electrodes	N/A	N/A	Electrode design	~ 6
P(VDF-TrFE) (This work)	**3D-architectured microelectrodes**	**10000**	**~ 5.2%**	**Electrode design**	**~ 7.7**

Notes: U is the output of the device after the enhancement strategy is used, and U_0 is the output of the device in the control experiment.

References

1. Shi, K. M.; Sun, B.; Huang, X. Y.; Jiang, P. K., Synergistic effect of graphene nanosheet and $BaTiO_3$ nanoparticles on performance enhancement of electrospun PVDF nanofiber mat for flexible piezoelectric nanogenerators. Nano Energy 2018, **52**, 153-162.
2. Shi, K. M.; Chai, B.; Zou, H. Y.; Shen, P. Y.; Sun, B.; Jiang, P. K.; Shi, Z. W.; Huang, X. Y., Interface induced performance enhancement in flexible BaTiO3/PVDF-TrFE based piezoelectric nanogenerators. Nano Energy 2021, **80**, 105515.
3. Zhou, Z.; Zhang, Z.; Zhang, Q.; Yang, H.; Zhu, Y.; Wang, Y.; Chen, L., Controllable Core-Shell $BaTiO_3$@Carbon Nanoparticle-Enabled P(VDF-TrFE) Composites: A Cost-Effective Approach to High-Performance Piezoelectric Nanogenerators. ACS Appl. Mater. Interfaces 2020, **12**, 1567-1576.
4. Deng, W. L.; Yang, T.; Jin, L.; Yan, C.; Huang, H. C.; Chu, X.; Wang, Z. X.; Xiong, D.; Tian, G.; Gao, Y. Y.; Zhang, H. T.; Yang, W. Q., Cowpea-structured PVDF/ZnO nanofibers based flexible self-powered piezoelectric bending motion sensor towards remote control of gestures. Nano Energy 2019, **55**, 516-525.
5. Hong, Y.; Wang, B.; Lin, W.; Jin, L.; Liu, S.; Luo, X.; Pan, J.; Wang, W.; Yang, Z., Highly anisotropic and flexible piezoceramic kirigami for preventing joint disorders. Sci. Adv. 2021, **7**, eabf0795.
6. Kim, S. R.; Yoo, J. H.; Kim, J. H.; Cho, Y. S.; Park, J. W., Mechanical and piezoelectric properties of surface modified (Na,K) NbO3-based nanoparticle-embedded piezoelectric polymer composite nanofibers for flexible piezoelectric nanogenerators. Nano Energy 2021, **79**, 105515.
7. Yuan, X. T.; Gao, X. Y.; Shen, X. Y.; Yang, J. K.; Li, Z. M.; Dong, S. X., A 3D-printed, alternatively tilt-polarized PVDF-TrFE polymer with enhanced piezoelectric effect for self-powered sensor application. Nano Energy 2021, **85**, 105985.
8. Zhang, L. L.; Gui, J. Z.; Wu, Z. Z.; Li, R.; Wang, Y.; Gong, Z. Y.; Zhao, X. Z.; Sun, C. L.; Guo, S. S., Enhanced performance of piezoelectric nanogenerator based on aligned nanofibers and three-dimensional interdigital electrodes. Nano Energy 2019, **65**, 103924.

Supplementary Figures

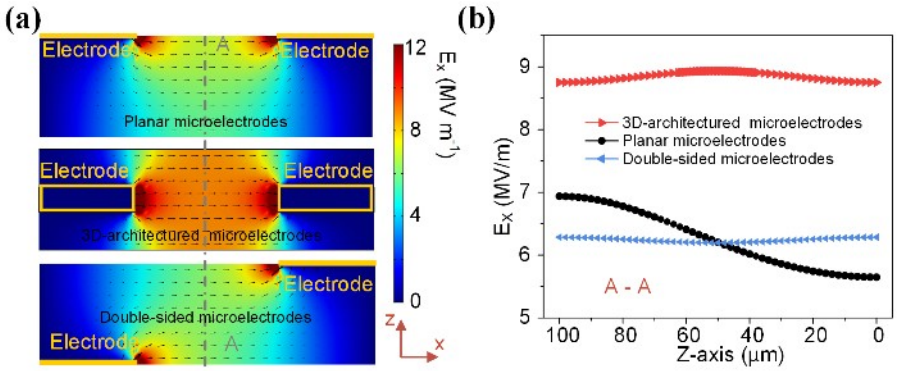

Figure S1. Effect of microelectrode layout on distribution of polarized electric field. (a) The simulated polarization electric field distribution in piezoelectric materials with three different electrode layouts: planar microelectrodes, 3D-architectured microelectrodes and double-sided microelectrodes. Model parameters: Length along x direction is 350 μm, thickness along z direction is 100 μm, electrode width is 100 μm and electrode spacing is 150 μm. (b) The x direction polarization electric field distribution of models with three different electrode layouts along the z direction in the middle position of the length direction. The simulation results show that the 3D-architectured microelectrodes have the optimal polarization electric field distribution.

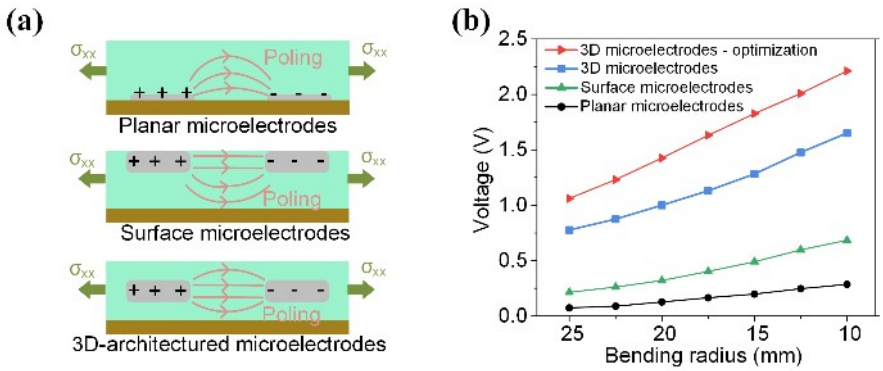

Figure S2. Effect of interdigital electrodes layout on piezoelectric performance. a) Three different electrode layouts are planar microelectrodes, surface microelectrodes and 3D-architectured microelectrodes. b) Piezoelectric output of piezoelectric films with three different electrode layouts. It is found that the piezoelectric performances are gradually improved with the gradual embedding of the electrodes into the piezoelectric materials (electrode width of 100 μm, electrode spacing of 150 μm and electrode depth of 23 μm). After optimization, the performance of 3D-architectured microelectrodes piezoelectric film can be further improved (the electrode width is 40 μm, the electrode spacing is 150 μm, and the electrode depth is 23 μm).

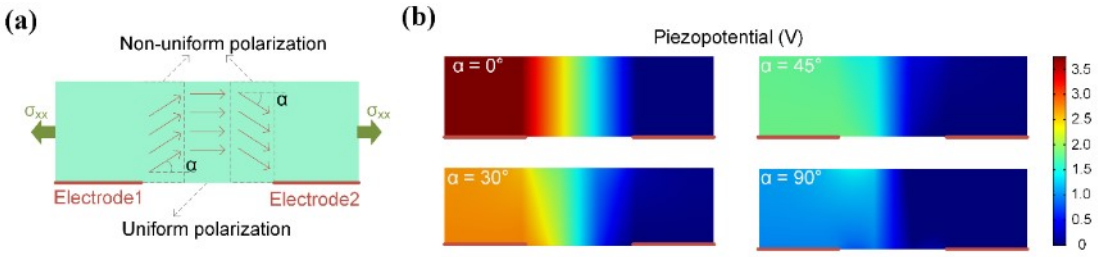

Figure S3. Piezoelectric performance under non-uniform polarization. a) A simplified treatment of piezoelectric devices with non-uniform polarization is made. The polarization part is divided into two parts: the non-uniform field with deflection angle of α and the uniform field with the direction of stress. b) With the increase of deflection angle α, the polarization field component along the stress direction decreases, and the piezoelectric output decays rapidly, indicating that reducing deflection angle α is helpful to improve the piezoelectric performance.

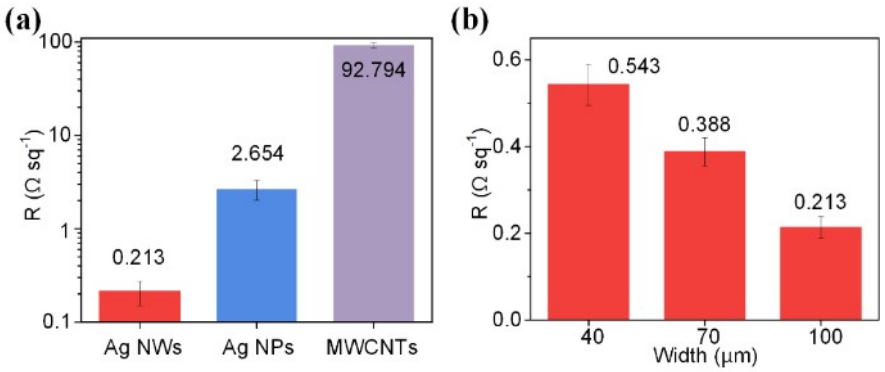

Figure S4. Sheet resistance of the 3D-architectured microelectrodes. (a) Sheet resistance of 3D-architectured microelectrodes with different conductive materials. Ag nanowires 3D-architectured microelectrode has the best electrical conductivity because of the high electrical conductivity of Ag and the interconnection of nanowires. (b) Sheet resistance of Ag nanowires 3D-architectured microelectrodes of different widths. It is found that with the decrease of electrode width, although the sheet resistance of the 3D-architectured microelectrodes increases, it still maintains good conductivity.

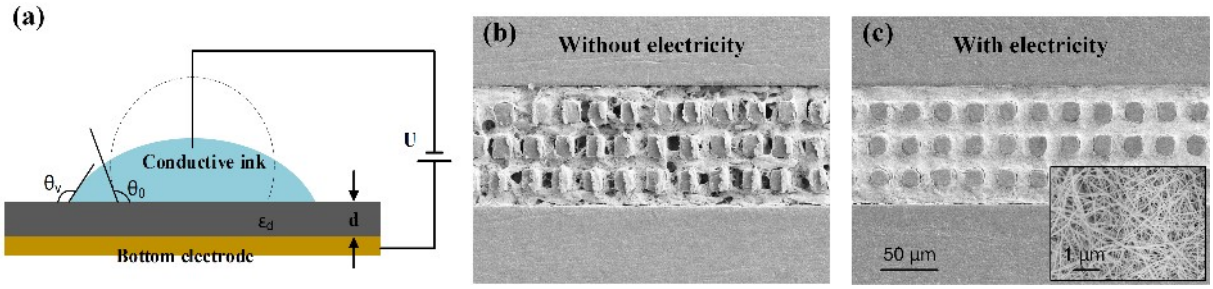

Figure S5. Electrowetting-assisted filling. a) Schematic diagram of electrowetting. The lower electrode is prepared at the bottom of the dielectric material, and the conductive droplet acts as the upper electrode. Applying high voltage alternating current between the upper and lower electrodes will significantly reduce the contact angle of the droplet on the material, which will make it easier to fill the conductive ink into the microchannels. b) The filling of conductive ink into microchannels without electricity. It is obvious that there are many cavity after filling, which will seriously affect the conductivity and stability of electrodes. c) The filling of conductive ink into microchannels with electricity. It is found that conductive materials can be filled full and dense in the microchannels, because the wettability of conductive materials in the microchannels is improved under the electric condition, which will significantly improve the stability of electrodes.

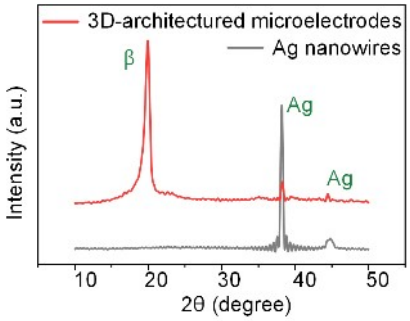

Figure S6. XRD patterns characterization. The gray curve is the XRD pattern of Ag nanowires, and the red curve is the XRD pattern of the 3D-architectured microelectrodes piezoelectric film. The results show that the piezoelectric film not only obtains obvious β peak, but also obtains weak Ag crystal direction peak, which indicates that it has good piezoelectric phase and has Ag nanowire embedded in the material.

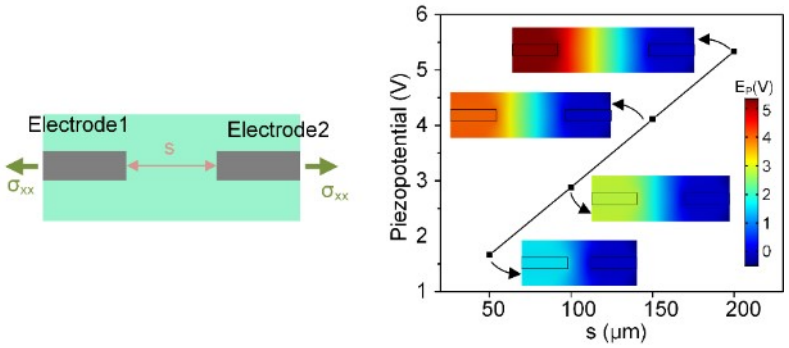

Figure S7. Effect of electrode spacing on piezoelectric performance. The diagram on the left is an illustration of the simulation model. The influence of electrode spacing on the piezoelectric output performance is analyzed by COMSOL simulation. The results show that the piezoelectric output is proportional to the electrode spacing. As a large electrode spacing requires a large polarization voltage, which increases the risk of electrical breakdown of the material, the electrode spacing of 150 μm is selected as a comprehensive consideration.

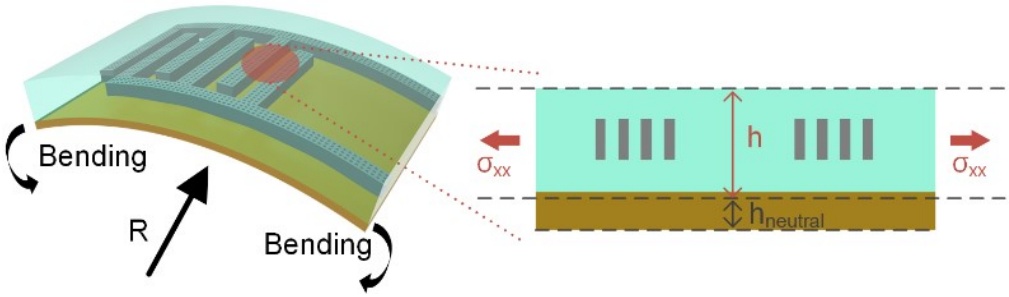

Figure S8. Mechanical analysis of bending process of 3D-architectured microelectrodes piezoelectric film. By mechanical matching of materials, the mechanical neutral plane (MNP) can be located in the substrate material, and the piezoelectric material will only be subjected to bending tensile stress. Since the bending stress is usually positively correlated with the distance from the MNP, we can simplify the simulation experiment so that the piezoelectric film only suffers a uniform bending tensile stress without considering the influence of substrate.

The MNP, located by the distance from the bottom surface of the multilayer structure, can be calculated as follows:

$$h_{neutral} = \frac{\sum_{i=1}^{N} \bar{E}_i h_i \left(\sum_{j=1}^{i} h_j - \frac{h_i}{2} \right)}{\sum_{i=1}^{N} \bar{E}_i h_i} \quad (1)$$

where $\bar{E}_i$ is the effective Young's modulus ($\bar{E}_i = E_i/(1-\nu_i^2)$, E_i is the Young's modulus and ν_i is

the Poisson's ratio of the i^{th} layer), h_i is the thickness of the i^{th} layer, and N is the total number of the layers. For the 3D-architectured microelectrodes piezoelectric film, the elastic property and thickness of each layer are as follows: $E_{kapton} = 4.56\ GPa$, $h_{kapton} = 50\ \mu m$, $E_{P(VDF-TrFE)} = 1.14\ GPa$, $h_{P(VDF-TrFE)} = 100\ \mu m$. The calculated MNP is located 33.3 μm above the bottom surface of the multilayered film, that is, in the kapton substrate. Therefore, the P(VDF-TrFE) piezoelectric film is completely stretched or compressed during the bending process, which will obtain a greater piezoelectric response.

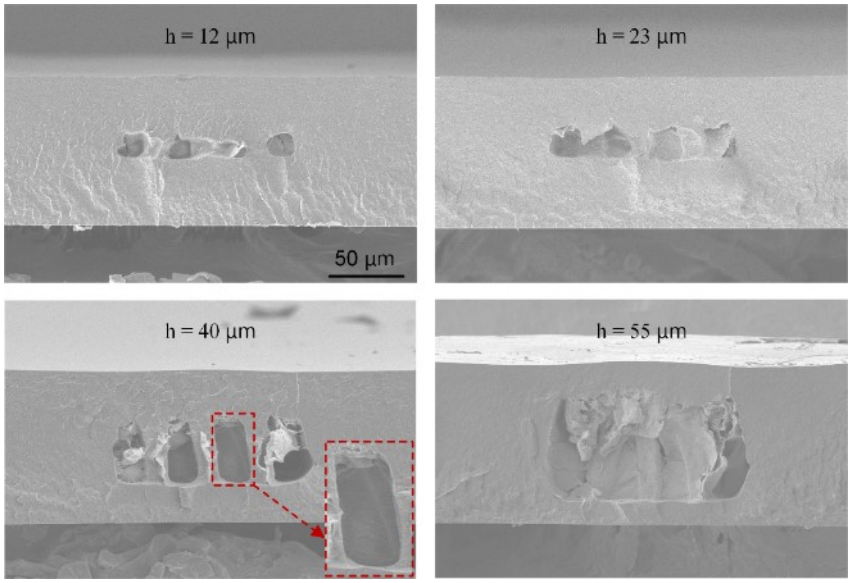

Figure S9. SEM images of 3D-architectured microelectrodes with different depths. The electrode depths are 12 μm, 23 μm, 40 μm and 55 μm, respectively. It can be seen that the conductive material is completely filled in the microchannels, and an integrated connection is formed between the micropillars and the encapsulation layer, realizing the controllable manufacturing of 3D-architectured microelectrodes with different depths. For the 3D-architectured microelectrodes with depth of 40μm and 55μm, part of Ag nanowires are pulled out during the process of making the cross section, but it is observed that the inside of the microchannels is still full filled.

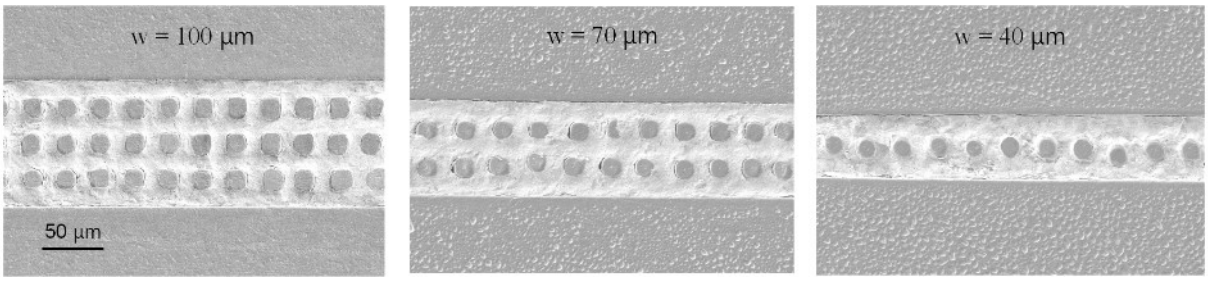

Figure S10. SEM images of 3D-architectured microelectrodes with different widths. The electrode widths are 100 μm, 70 μm and 40 μm, respectively. The full filling of 3D-architectured microelectrodes in microchannels of different widths is realized, and the micropillars maintains a good morphology, which contributes to the realization of integrated encapsulation and the improvement of electrodes stability.

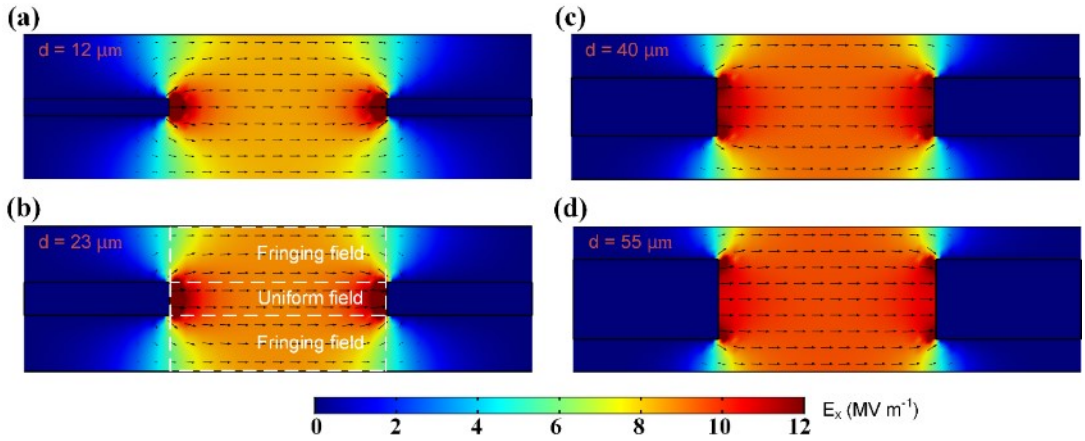

Figure S11. Effects of 3D-architectured microelectrodes with different depths on the polarization field distribution of piezoelectric materials. Simulation of polarization electric field distribution at electrode depths of (a) 12 μm, (b) 23 μm, (c) 40 μm and (d) 55 μm, respectively. It is found that with the increase of electrode depth, the polarization field distribution in the piezoelectric material is gradually uniform, and the polarization field strength is gradually enhanced. It is obvious that more uniform field regions are obtained and less fringing field exists, which will allow more piezoelectric materials to participate in the piezoelectric response in d_{33} mode. Therefore, the deeper the electrode depth, the stronger the polarization effect.

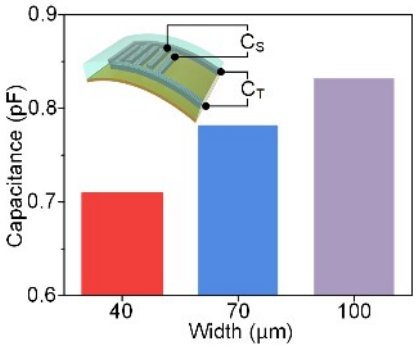

Figure S12. Capacitance between electrode pairs in a 3D-architectured microelectrodes. The test results show that with the decrease of electrode width, the capacitance between electrode pairs decreases, which will improve the output response of piezoelectric devices. The capacitance between electrode pairs can be obtained from the formula $C_S=C_T/N$ (where C_S is the capacitance between electrode pairs, C_T is the total capacitance of the piezoelectric device, and N is the number of electrode pairs).

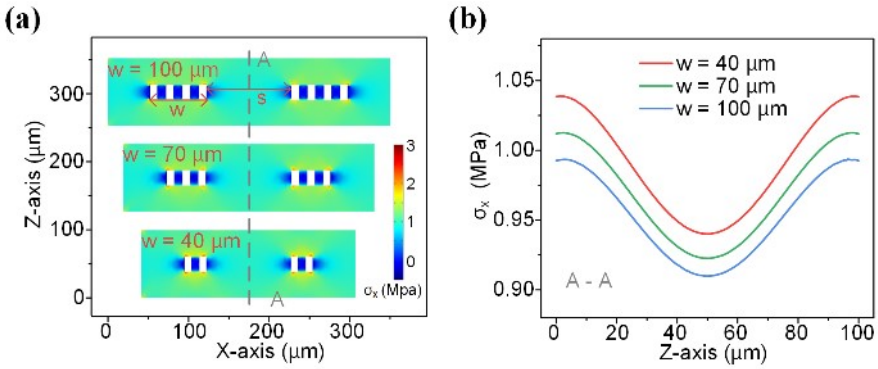

Figure S13. Effect of 3D-architectured microelectrodes width on bending stress distribution. (a) Stress distribution of piezoelectric materials with 3D-architectured microelectrodes of different widths under the same bending deformation. It can be found that with the decrease of electrode width, the stress distribution between electrode pairs becomes more uniform. (b) Bending stress distribution along the x-axis in the middle of electrode pairs for piezoelectric materials with different electrode widths. It is found that with the decrease of the electrode width, the proportion of the effective piezoelectric material increases ($s / (w + s)$), and more stress is concentrated in the effective region. It can be seen from the stress-charge formula ($D= d_{ij}\sigma$, where D is the electrical displacement, d_{ij} is the piezoelectric coefficient and σ is the stress) of piezoelectric effect that with the increase of stress, a larger piezoelectric output will be obtained.

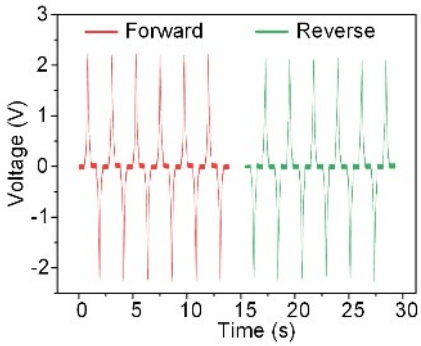

Figure S14. Switching polarity test of piezoelectric devices. The stable output response of the piezoelectric device is obtained by the bending test of the forward and reverse connection, which indicates that the device obtains the real piezoelectric output and has excellent anti-interference.

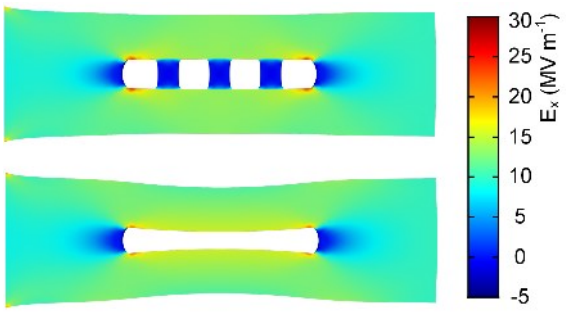

Figure S15. Mechanical interlocking of meshed microelectrodes. Stress distribution and deformation of microelectrodes with and without meshed micropillars under bending action. It is obvious that the microelectrodes with meshing micropillars can obtain relatively uniform stress distribution and small deformation, which improves the electrodes stability.

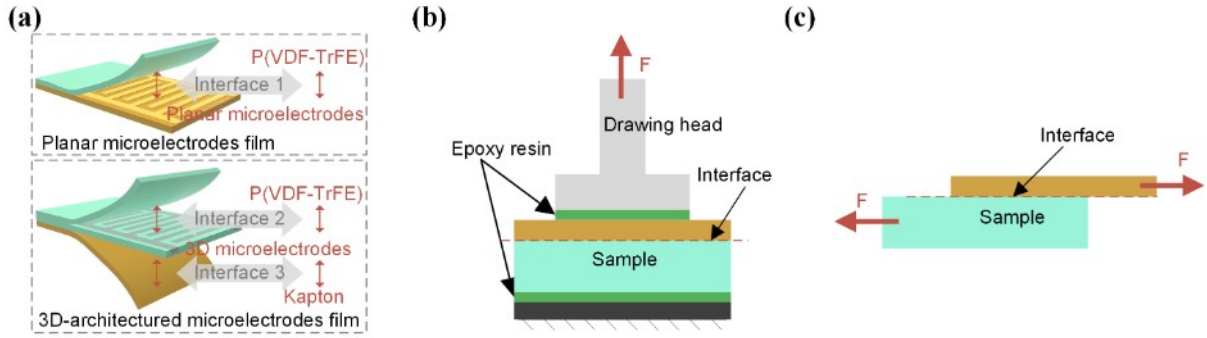

Figure S16. Interface distribution and interface bonding strength test method of piezoelectric devices. (a) Different interface distribution of planar microelectrodes piezoelectric device and 3D-architectured microelectrodes piezoelectric device. (b) Test diagram of tensile strength of different interfaces. The sample is bonded to the fixed end and the drawing head by epoxy resin, and then the bonding strength of the interface is tested by a stretching machine. (c) Test diagram of sheer strength of different interfaces. Mechanical testing machine model is ESM303 (Mark-10).

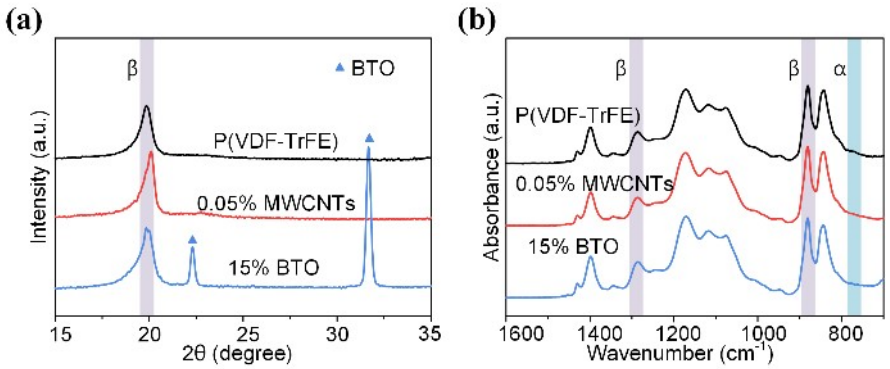

Figure S17. Characterization of composite films. (a) X-ray diffraction (XRD) scattering pattern of composite film and pure P(VDF-TrFE) film. (b) Fourier transform infrared (FTIR) spectra of composite film and pure P(VDF-TrFE) film.

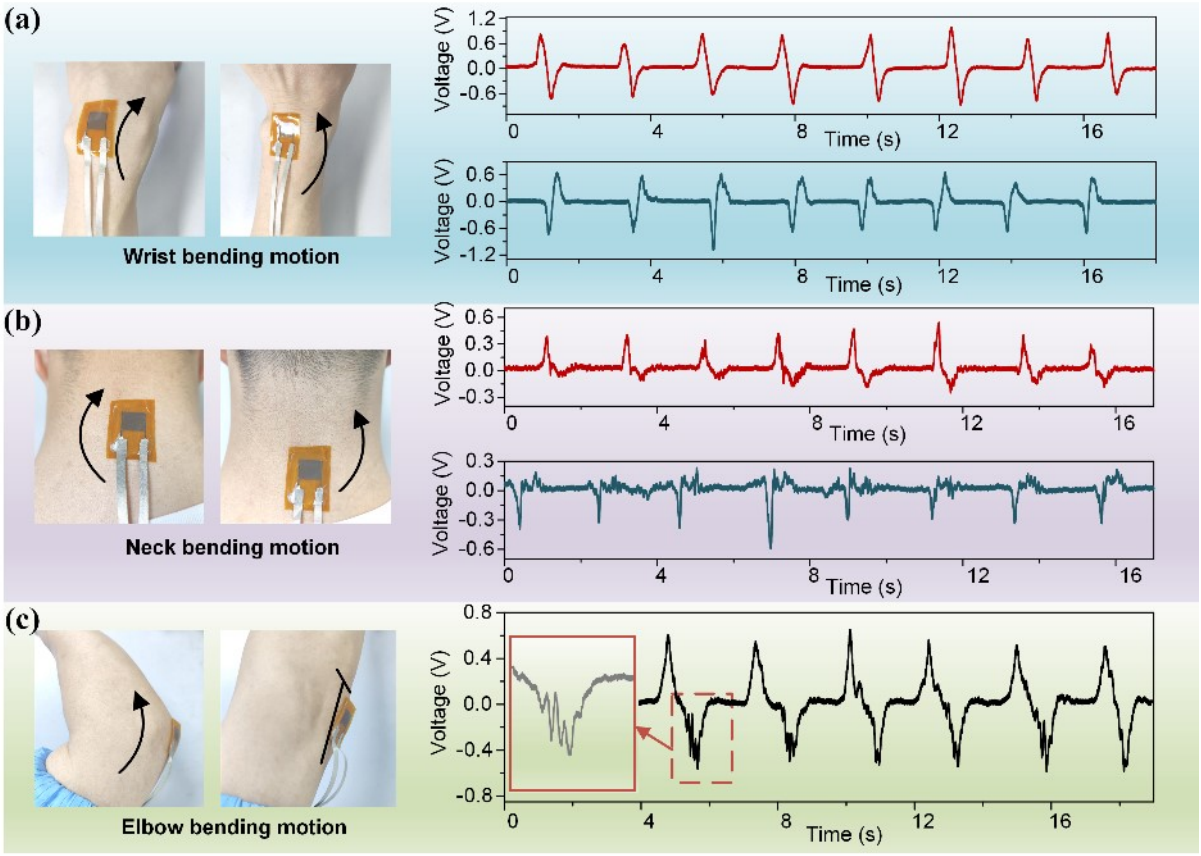

Figure S18. Real-time monitoring of different joint motions. Monitoring of bending motions of the (a) wrist, (b) neck and (c) elbow. The results show that the developed device can monitor the motion of different joints very well.

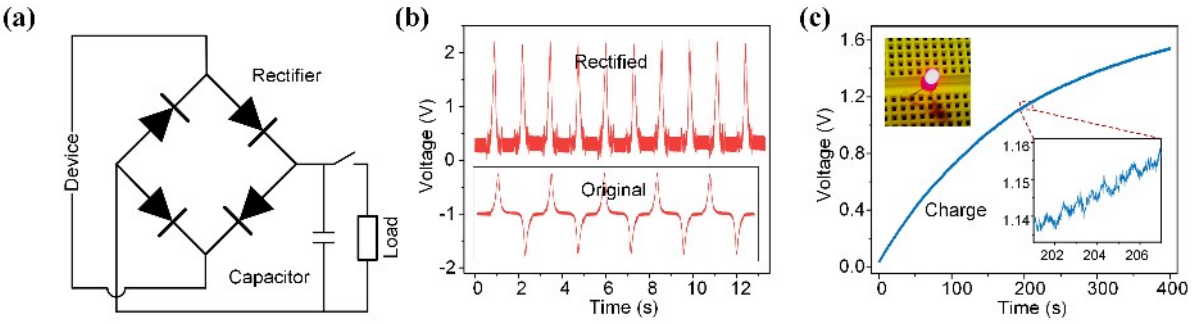

Figure S19. Energy harvesting of devices in low frequency bending motion. (a) Rectifier circuit diagram of device for energy harvesting. (b) The output signal of the device before and after rectification. (c) The charge curve of the capacitor （2.2pF） at low frequency and the parallel connection of the two capacitors successfully light an LED. Although the charging process is relatively slow, it is a low-frequency energy harvesting consistent with human movement.

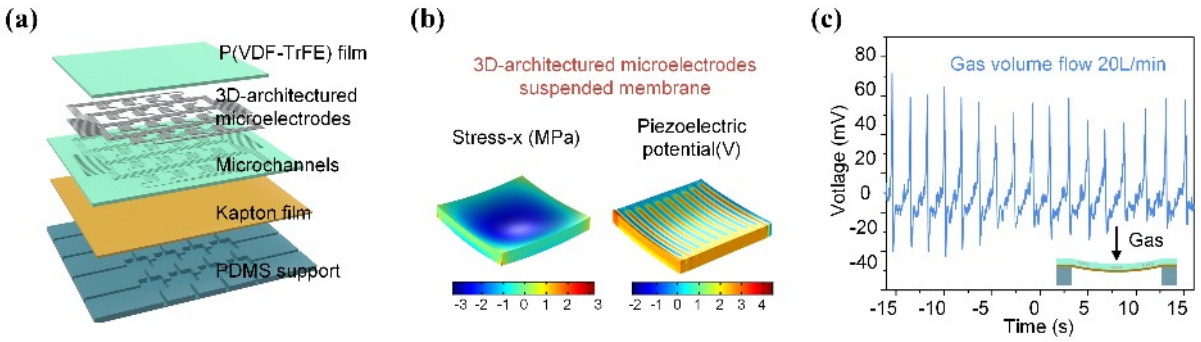

Figure S20. 4 × 4 pressure sensor array based on suspended membrane. (a) Structural explosion diagram of pressure sensor array based on suspended membrane. The sensor array is composed of PDMS support layer, kapton substrate, microchannels, 3D-architectured microelectrodes and encapsulation layer. (b) Simulation of stress distribution and piezoelectric potential for 3D-architectured microelectrodes piezoelectric film pressure sensor based on suspended membrane. The result show that the suspended membrane structure can convert the vertical force into the in-plane stress of the piezoelectric film. This suspended membrane structure proved to be more sensitive to axial forces. (c) The 3D-architectured microelectrodes pressure sensor based on a suspended membrane is used for airflow sensing.

Captions for Supplementary Movies

Video S1

Application example of gesture remote control. The 3D-architectured microelectrodes piezoelectric film is attached to the finger, and the signal is collected and processed by the Arduino development board to realize the remote control of the manipulator.